Earth Planet. Sci. Lett. 653 (2025) 119213

Contents lists available at ScienceDirect

Earth and Planetary Science Letters

journal homepage: www.elsevier.com/locate/epsl

Record of de-serpentinization and re-serpentinization of an exhumed slab sliver: Implications for fluid circulation in subduction zones

Damián Donoso-Tapia [a], Kennet E. Flores [a,*], Celine Martin [b,c], Sarah Hull [a],
David Hernández-Uribe [d], Esteban Gazel [e]

[a] Department of Earth, Marine and Environmental Sciences, University of North Carolina, Chapel Hill, NC 27599, USA
[b] Department of Earth and Planetary Sciences, American Museum of Natural History, New York, NY 10024, USA
[c] Lamont Doherty Earth Observatory, Columbia University, Palisades, NY 10964, USA
[d] Department of Earth and Environmental Sciences, University of Illinois Chicago, Chicago, IL 60607, USA
[e] Department of Earth and Atmospheric Sciences, Cornell University, Ithaca, NY 14853, USA

ARTICLE INFO

Keywords:
Subduction zones
Ultramafic rocks
Eclogites
De-serpentinization
Re-serpentinization
Boron isotopes

ABSTRACT

Fluid release associated with serpentinite dehydration (de-serpentinization) during subduction plays a key role in fundamental geological processes such as element transport and recycling, seismicity, and arc magmatism. Although the importance of these fluids is well-known, evidence of de-serpentinization remains scarce in the rock record. Here, we investigated the effects of de-serpentinization and fluid circulation in exhumed metaperidotites from the Raspas Complex (Ecuador). This Early Cretaceous complex records warm subduction (~13.5 °C/km) and has been hypothesized to represent a coherent slab sliver that preserves the mantle-crust contact (moho) between eclogite-facies metaperidotites and the corresponding crustal section. Petrological observations reveal that titanian-clinohumite-bearing metadunites and banded metaperidotites underwent de-serpentinization after reaching peak pressure–temperatures (*P*–*T*) of ~1.3–1.6 GPa and 620–650 °C. The peak paragenesis is partially obscured by a strong retrograde overprint, driven by crust-derived metamorphic fluids ($\delta^{11}B \sim -6$ to $+8$ ‰) that infiltrated at varying fluid/rock ratios, triggering the re-serpentinization of metaperidotites during exhumation ($P < 1.3$ GPa and 320–400 °C). Thermodynamic forward modeling reveals that fluid release in the Raspas paleo-subduction zone is controlled by brucite breakdown and de-serpentinization, which occur at depths of 25–30 km and ~50 km, respectively, accounting for a total of up to 10 wt. % H_2O of water stored in the rock. Comparatively, dehydration of the crustal section, albeit a minor component, promotes enhanced fluid circulation between 25 and 45 km. During exhumation, circulating crust-derived metamorphic fluids heavily metasomatized the ascending slab sliver and effectively modified its geochemical signature. The depth range of the dehydration reactions overlap the depth of non-volcanic tremors and slow-slip events in warm, active subduction zones worldwide (25–65 km). Thus, the Raspas Complex offers an *in-situ* window into the fluids responsible for triggering these seismic events.

1. Introduction

The subduction of serpentinized mantle is key for different fundamental processes at convergent boundaries. Along with the transport of water and other volatiles deep into the Earth, dehydration of serpentinized slab peridotites (hereinafter referred to as de-serpentinization) contributes to element cycling, seismicity, and arc magmatism (e.g., Condit et al., 2020; Evans et al., 2013; Gutiérrez-Aguilar et al., 2022). These slab serpentinite-derived fluids have been suggested to be responsible for the oxidized nature of arc magmas (Zhang et al., 2021), although this interpretation is debated (e.g., Ague et al., 2022; Piccoli et al., 2019). Yet, despite the importance of fluids derived from slab de-serpentinization, evidence of this process recorded in the geological record is scarce.

Deeply exhumed slab slivers offer empirical evidence of their fate during subduction and exhumation. However, upper mantle sections are usually incomplete, dismembered, and often tectonically juxtaposed to lithospheric sections (e.g., Angiboust et al., 2009; Scambelluri et al.,

---

* Correspondence author at: 104 South Road, CB #3315, Chapel Hill, NC 27599-3315, United States.
E-mail addresses: damiandt@email.unc.edu (D. Donoso-Tapia), keflores@unc.edu (K.E. Flores), cmartin@amnh.org (C. Martin), sbrookw@live.unc.edu (S. Hull), davidhu@uic.edu (D. Hernández-Uribe), egazel@cornell.edu (E. Gazel).

https://doi.org/10.1016/j.epsl.2025.119213
Received 25 September 2024; Received in revised form 9 January 2025; Accepted 11 January 2025

2014). In the Betic Cordillera, the Nevado-Filábride Complex recorded a prograde transition from antigorite-serpentinite to chlorite-metaharzburgite, suggesting a complete de-serpentinization at peak pressure–temperature (*P*–*T*) of 1.6–1.9 GPa of 680–710 °C (e.g., Padrón-Navarta et al., 2011; Trommsdorff et al., 1998). Similarly, chlorite-metaharzburgites and garnet peridotites from the Alpine Cima di Gagnone suite are hosted in a mélange and regarded as slab fragments that record slab de-serpentinization and chlorite dehydration at peak conditions of <3 GPa and 750–850 °C (Scambelluri et al., 2014). Partial de-serpentinization of ultramafic rocks at peak conditions of 3.2–4.2 GPa and 520–540 °C have been reported in the high- to ultra-high pressure (UHP) suite in the Changawuzi area of southwestern Tianshan. A retrograde re-serpentinization stage during exhumation is also interpreted from the breakdown of Ti-chondrodite into Ti-clinohumite + Olivine + Antigorite (Shen et al., 2015). Another example of partial de-serpentinization has been described in the high-pressure (HP) Zermatt-Saas ophiolite in the western Alps, where Ti-chondrodite-bearing metaperidotites attained peak conditions of 2.8–3.5 GPa and 600–670 °C (Luoni et al., 2018). This complex preserves an intricate metamorphic olivine vein network associated with incipient antigorite dehydration (Kempf et al., 2020; Ulrich et al., 2024).

In the upper mantle section and along an apparent mantle-crust contact (moho) of the Andean Raspas Complex (Fig. 1), de-serpentinization and intense fluid-rock interaction have been proposed based on the occurrence of metamorphic olivine- and Ti-clinohumite-bearing metaperidotites, chlorite-metaharzburgites with a spinifex-like texture resembling dehydrated serpentinites, and fluid inclusion-rich zoisite and vesuvianite-bearing vein rocks and eclogites (Gabriele, 2002; Halama et al., 2013; Herms et al., 2012). This Early Cretaceous complex is hypothesized to represent a coherent slab section that preserves its mantle and crustal sequences and records warm subduction, reaching peak eclogite facies (da Silva et al., 2023; Feininger, 1980; John et al., 2010). Much of the work has been carried out on the crustal sections of the Raspas Complex, albeit the ultramafic lithologies are of key importance in the release of fluids upon antigorite dehydration. Therefore, this unique exposure thus represents a unique natural laboratory to study the petrological and geochemical record of de-serpentinization, fluid release, and subsequent retrograde fluid-rock interaction on an exhumed slab section. In this contribution, we present mineral chemistry, whole-rock geochemistry, and *in-situ* boron isotope data on a set of ultramafic samples collected in an open pit quarry near the Tahuín Dam (Ecuador). We couple these results with forward thermodynamic models of different key lithologies within the Raspas Complex to shed light into slab dehydration and fluid circulation in

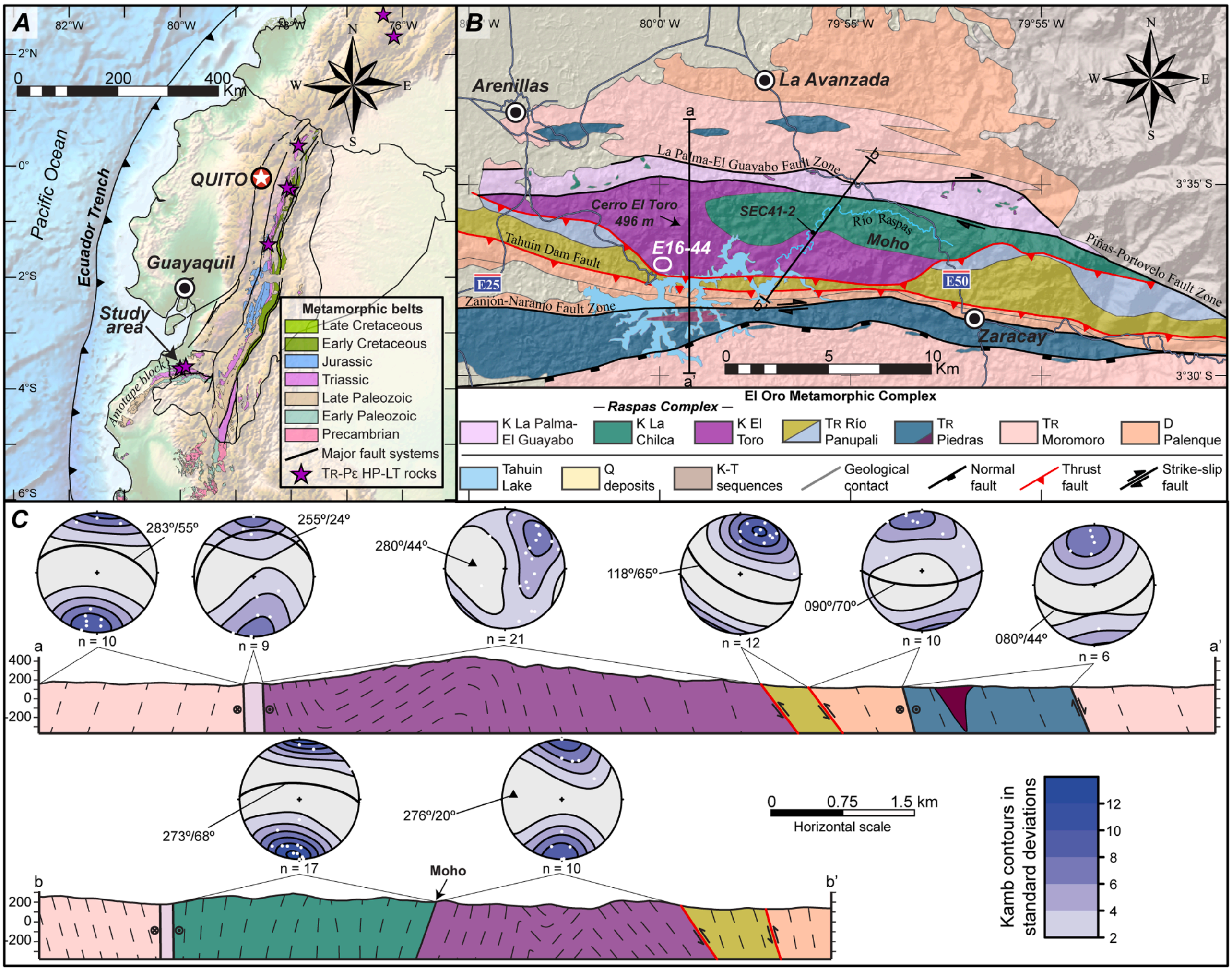

Fig. 1. Overview of the Raspas Complex. A. Map of Ecuadorian Andes displaying the metamorphic belts and major fault systems. B. Geologic map of the northern section of the El Oro Metamorphic Complex. The white oval indicates the location of the Tahuin Quarry Dam, where the samples were collected. C Geologic cross-sections through the Raspas Complex displaying its highly folded nature (dash lines show apparent dips of foliation). Stereonets are equal-area, lower hemisphere projections depicting contoured poles to foliation within each unit along the profiles. Great circles represent the average foliation planes, and black triangles represent the fold hinge within the El Toro unit. Maps and structural features after Aspden et al. (1995); Donoso-Tapia et al. (2024); Egüez and Gaona (2017); Gabriele (2002); INGEMMET (2022); and Litherland (1994).

subduction zones.

2. The Raspas complex

The Raspas Complex is a fault-bounded, Early Cretaceous metamorphic sequence within the El Oro Metamorphic Complex exposed in the Amotape block in southwest Ecuador (Fig. 1A-B). This block has been interpreted as an allochthonous accreted continental terrane during the Early Cretaceous or as a para-autochthonous domain displaced northward and juxtaposed to the Gondwana margin in the Cretaceous (Bellido et al., 2009; Mourier et al., 1988). The Raspas Complex is interpreted as a complete exhumed oceanic crust section that preserves all slab components (i.e., ultramafic, mafic, and sedimentary layers). The lower unit comprises meta-ultramafic rocks with varying degrees of serpentinization often cut by mafic dikes (El Toro unit). The upper section (La Chilca unit or Raspas Formation) consists of eclogites and mafic blueschists locally interlayered with garnet-chloritoid-kyanite metapelites (Aspden et al., 1995; Feininger, 1980; Gabriele et al., 2003). The contact between the uppermost mantle and oceanic crust (moho) is exposed in the Raspas River (Fig. 1B).

Petrochronological constraints on eclogites and metapelites indicate that the eclogite-facies peak occured at ca. 130 Ma, followed by exhumation to shallower crustal levels at ca. 129–123 Ma (da Silva et al., 2023; Gabriele, 2002; John et al., 2010). Previous peak *P-T* conditions were determined using conventional thermobarometry and chemographic projections, yielding *P-T* conditions of ~2.0 GPa and ~550–600 °C for the metapelites, and ~1.6 GPa and ~600 °C for the eclogites (Gabriele et al., 2003; John et al., 2010). Blueschists have been interpreted as retrogressed eclogites that record an amphibolite-facies overprint at 1.4–1.6- GPa and ~600 °C (John et al., 2010). Recent *P-T* estimates derived from thermodynamic modeling and Zr-in-rutile thermometry suggest a prograde *P-T* path from ~1.4 GPa and ~600 °C to ~1.6 GPa and ~660 °C, followed by an isobaric heating phase to ~710 °C (da Silva et al., 2023).

Geochemical studies of Raspas rocks indicate that the blueschists and eclogites were derived from a subducted oceanic plateau (Arculus et al., 1999; Bosch et al., 2002; da Silva et al., 2023). Contrarily, it is also argued that the crustal rocks were part of subducted seamounts, while the metaperidotites may represent depleted, MORB-like mantle rocks, both layers interpreted as representing a coherent, exhumed HP ophiolite suite (John et al., 2010; Urann et al., 2020). Nevertheless, in both scenarios it is argued that it corresponds to an anomalous, thickened oceanic crust.

The occurrence of chlorite-harzburgites and zoisite- and vesuvianite-bearing sections within metaperidotites, dikes, and eclogites have been linked to de-serpentinization, fluid circulation, and intense fluid-rock interactions. Initial strontium isotope ratios and rare earth element (REE) contents in metaperidotites indicate an intense hydrothermal alteration at or near the seafloor during initial serpentinization. By contrast, whole-rock oxygen isotopes yield inconclusive data, as they indicate that serpentinization took place at low temperatures or was driven by a high $\delta^{18}O$ fluid, comparable to $\delta^{18}O$ values obtained in HP zoisite-bearing eclogites in the study area (Halama et al., 2011; 2013). Two types of eclogites have been identified in the El Toro dikes and La Chilca unit and have been grouped as MORB- and zoisite-type. Both record an intense HP metasomatic overprint with contrasting geochemical signatures. Radiogenic and stable isotopes (Sr, Nd, Ni, Li, O) and fluid inclusion analysis suggest that metasomatism was triggered by externally sourced low salinity fluids associated with the dehydration of oceanic crust or a mixture of fluids sourced from metasediments and serpentinites (Halama et al., 2010; 2011; 2013; Herms et al., 2012).

Serpentine polymorphs and other mineral phases were differentiated by Raman microscopy at Cornell University, while mineral phase compositions were obtained by electron-probe microanalyzer (EMPA) at the American Museum of Natural History. In-situ boron isotopes were measured by LA-MC-ICP-MS at the Lamont Doherty Earth Observatory, following the method developed by Martin et al. (2015). Thermodynamic phase equilibria and forward modeling were done using Perple_X software, version 6.9.1 (Connolly, 2005). A detailed description of the methodology is included in Appendix 1 Supplementary Material (SM) along with supporting figures, tables, and data. Collected analytical data is reported in the Data Sets S1–3, which can also be found at EarthChem Library – Repository, an open-source online data repository for geochemical datasets (Donoso-Tapia et al., 2025a, b, c). Mineral abbreviations follow those suggested by Warr (2021).

3. Field observations

The El Toro and La Chilca units crop out along a highly deformed E-W belt bounded by a dextral-shear zone in the north, and a southward dipping thrust fault in the south (Fig. 1B). Analysis of existing foliation data (Table S1) indicates that the Raspas Complex is structurally distinct to the surrounding units. Foliation within both units generally strikes E-W with steep north and south dips (~90–60°) within La Chilca, and large variations in the dip angle (~90–30°) from north to south within El Toro. Foliation analysis within the El Toro unit shows large-scale folds with hinges of 280°/44° in the west and 276°/20° in the east (Fig. 1C).

Exposures of the El Toro metaperidotites are limited to scattered quarries, creeks, and outcrops along the Raspas River (Fig. 1B). The Tahuín Dam open pit quarry (3°37′1.33″ S - 80° 0′0.51″ W, Fig. S1) offers a unique window into the El Toro unit, where the outcrop is highly deformed and displays a well-developed foliation. In the southern wall of the quarry, metadunites and banded metaperidotites are locally folded, intruded by metagabbroic dikes, and cut by west-dipping reverse faults (Fig. 2A-C). In the northern section, a high-angle west-dipping fault separates foliated metadunites and minor metaclinopyroxenites from olivine-bearing serpentinites (Fig. 2D). Modal estimates of the lithologies in the quarry show that metadunites are the most common rock exposed (~85 %, Fig. 2F), albeit with varying degrees of foliation and folding, followed by banded metaperidotites (~10 %, Fig. 2G-H) and serpentinites (~5 %).

4. Petrology

Representative thin-section scans and additional figures are provided in the appendix SM1. Electron microprobe analyzer (EMPA) mineral chemistry is given in dataset S1. Metadunites are characterized by a high modal proportion of olivine granoblasts (generally 60–90 %) and scarce pyroxenes and amphiboles (Fig. 2F, Fig. 3). Folded and foliated metadunites often contain antigorite-rich domains and sheared olivine aggregates (Fig. S2). Accessory minerals include spinel, Ti-clinohumite (only in sample 44–6), diopside, amphibole, and chlorite. Antigorite was identified through Raman spectroscopy and it is the main serpentine polymorph, displaying the typical well-defined shoulder in the 550–670 cm^{-1} region and double peaks in the high wavenumber region at c. 3670 and 3710 cm^{-1} (Fig. S7). It occurs as inclusions in olivine, interstitial networks around olivine, and retrograde veins that crosscut the olivine-rich assemblage.

Banded metaperidotites are mainly composed of three alternating bands (Fig. 2G-H; Fig. S3); the first is an olivine-rich band that grades into a transitional zone marked by the appearance of rusted olivine grains that leads into a second antigorite-rich (± amphibole) band with no olivine. The third band comprises diopside-amphibole-chlorite (Di-Amp-Chl band) and has a sharp contact with the antigorite-rich band. The olivine-rich bands constitute most of the banded assemblage and are composed of pristine to heavily altered/rusted olivine and antigorite with accessory Ti-clinohumite (± ilmenite), spinel, chlorite, diopside, amphibole, and apatite (Fig. 4A). The antigorite bands have accessory diopside, amphibole, and rare spinel relics, whereas the Di-Amp-Chl bands consist of pseudo-spinifex to anhedral diopside grains overgrown by amphibole in a chlorite-rich matrix (Fig. 4B). Minor Di-Amp and Di-Chl bands only occur in samples 44–2 and 3, respectively.

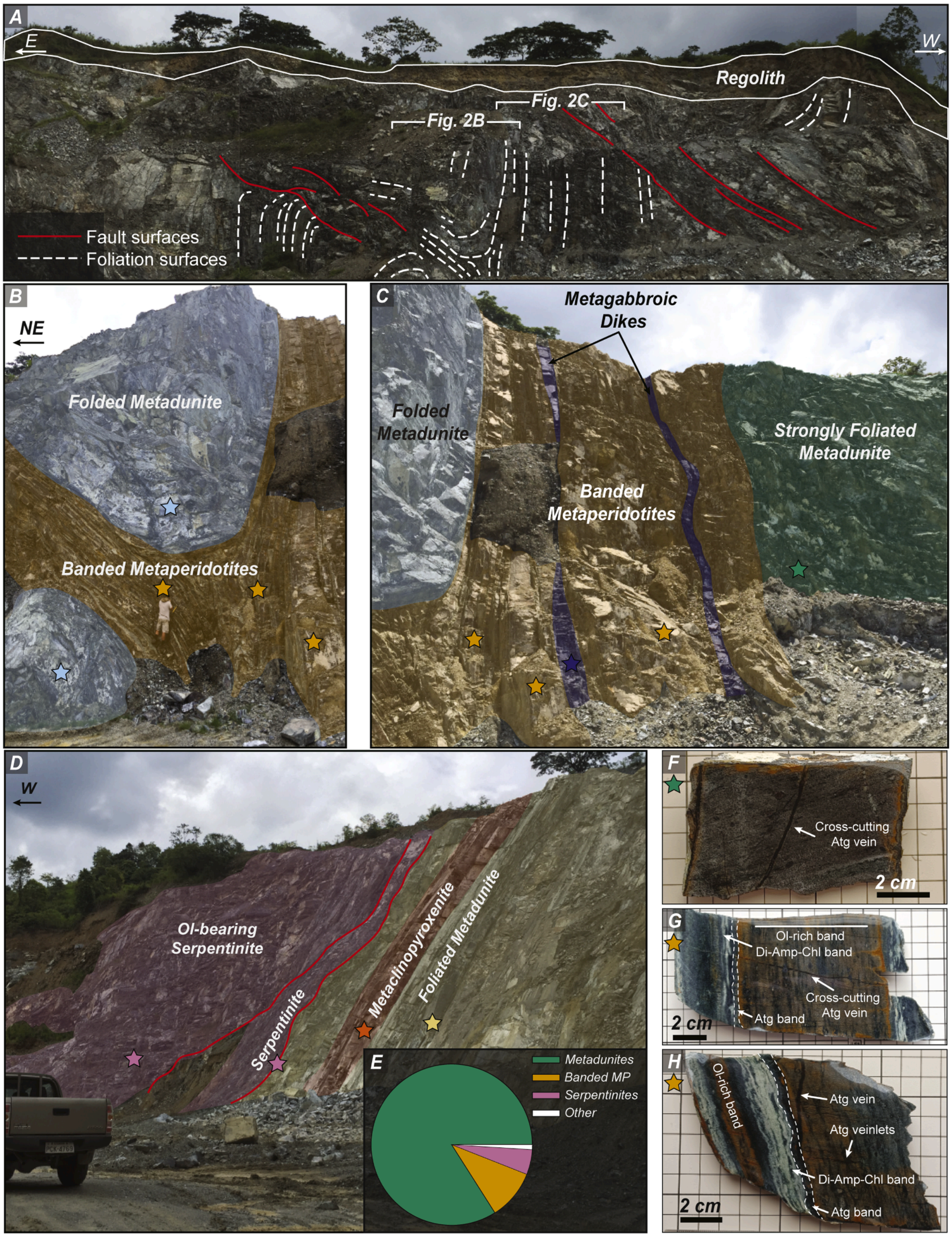

Fig. 2. Representative features of the Tahuín Dam Quarry. A. Main faults and foliation surfaces found in the southern sector of the quarry. B-C. Rock assemblages found in the southern sector. D-E. Rock associations of the northern sector of the quarry and estimated modal proportion of the lithologies throughout the outcrops. F. Hand specimen of a highly foliated metadunite (sample 44–8). G-H. Hand specimens of banded metaperidotites (samples 44–4 and 3, respectively). The colored stars represent the sampling points.

Retrograde antigorite occurs as veins crosscutting the observed banding.

The metaclinopyroxenite (44–10) consists of moderately to heavily altered diopside within a chlorite-rich matrix. A chlorite vein cuts through the main assemblage and is accompanied by carbonate, amphibole, magnetite, and garnet.

An antigorite-rich matrix dominates the serpentinites. Sample 44–11 has a massive texture and over 95 % modal antigorite, whereas sample 44–12 has a strong foliation preserved in sheared spinel and olivine grains (Fig. S3). Olivine veinlets are rare and typically do not exceed ~2 mm in length. Accessory phases include spinel grains that contain antigorite, chlorite, and garnet inclusions in the magnetite rims and are associated with small Ni-silicate overgrowths. Other retrograde features include a diopside vein with amphibole overgrowths (44–11) and discrete chrysotile and magnesite veinlets (44–12).

The metagabbroic dike (44–1) is porphyroblastic and consists of an amphibole matrix with associated omphacite, vesuvianite, and titanite (Fig. S3). Amphibole crystals are optically zoned with orange cores and blue rims under plane polarized light. Omphacite is rich in fluid inclusions and contains blue amphibole patches overgrowths. Vesuvianite occurs as elongated or round grains and contains titanite, omphacite, and amphibole inclusions.

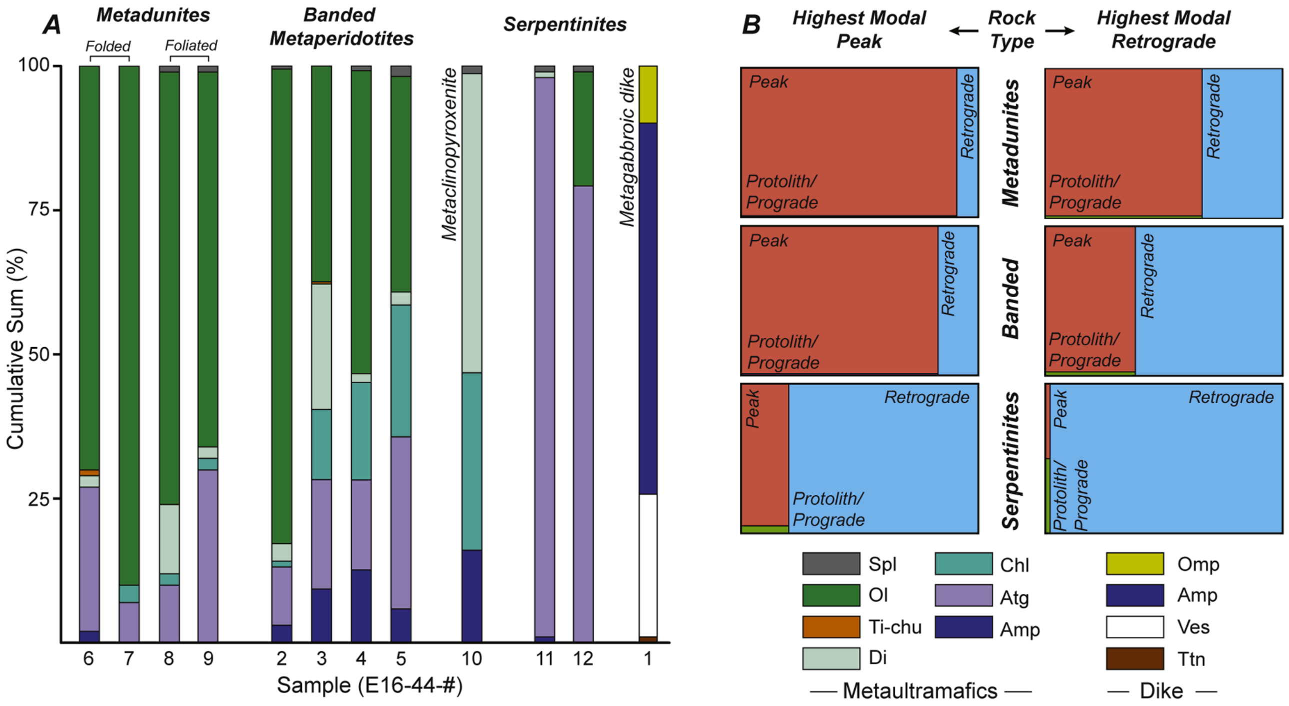

Fig. 3. Mineral assemblages of the Tahuin Quarry Dam sample suite. A. Mineral modal proportion estimated for the collected samples. B. Relative proportion between protolith/prograde, peak, and retrograde phases.

4.1. Mineral chemistry

Spinel cores and rims are classified as Fe-chromite and Cr-magnetite, respectively (Fig. S4). The cores are heavily depleted in Mg ($\#Mg = Mg/(Mg+Fe^{2+}) = 0.10–0.22$) and Al ($\#Cr = Cr/(Cr+Al) = 0.72–0.99$) but have TiO_2 and MnO contents up to 3.9 wt. % and 2.1 wt. %, respectively. By contrast, the rims and individual magnetite grains are enriched in ferric iron ($\#Fe^{3+} = Fe^{3+}/(Cr+Al+Fe^{3+}) = 0.74–1.00$) and depleted in TiO_2 and MnO (0.2–2.1 wt. % and 0.0–0.4 wt. %, respectively) relative to the cores.

Three main types of olivine occur in the metaperidotites (Fig. 4C). Zoned olivine is present in banded metaperidotites (samples 44–2 to 5) and a folded metadunite (sample 44–6), they display a core-to-rim zonation coupled with a decrease in X_{Mg} ($X_{Mg} = Mg/(Mg+Fe)$; 0.87–0.91 in cores, 0.82–0.89 in rims) and increase in MnO (0.10–0.21 wt % in cores, 0.19–0.50 wt. % in rims). Unzoned olivine occurs in folded (sample 44–7) and foliated (sample 44–9) metadunites, and serpentinite 44–12. These have a narrow X_{Mg} range between 0.88 and 0.90 and MnO contents overlap those of olivine cores and rims (0.14–0.31 wt. %). Highly sheared olivine aggregates are in banded metaperidotites, the strongly foliated metadunite 44–8, and serpentinite 44–12; their X_{Mg} is comparable to olivine rims (0.85–0.88), whereas MnO contents range from 0.19 to 0.32 wt. %. These aggregates typically contain sheared antigorite inclusions and display a well-developed antigorite outer rim.

Ti-clinohumite may contain chlorite inclusions or rims consisting of metamorphic olivine and ilmenite (Fig. 4A). TiO_2 contents range between 3.8 and 6.4 wt. %, while fluorine (F) measurements were below the detection limits (~0.1 wt. %).

The clinopyroxenes are mainly classified as diopside ($En_{48–36}Wo_{50–34}Fs_{7–0}$) in metaperidotites and omphacite ($Jd_{52–39}Aeg_{13–4}Quad_{52–41}$) in the metagabbro, based on Morimoto (1988) (Fig. S5A). The X_{Mg} has a narrow range in banded, massive, and serpentinite samples (0.92–0.96) and is negatively correlated with Al_2O_3 concentrations, except for two augite cores within pseudo-spinifex diopside in 44–3 that show lower X_{Mg} (0.78–0.83) (Fig. 4C). In the metaclinopyroxenite, X_{Mg} is lower (0.86–0.91) and not correlated to Al_2O_3. Diopside contents of Al, Cr, Ti, and Na are positively correlated, and some grains may display a concentration gradient in these elements between the center of the crystal and the border. By contrast, pseudo-spinifex diopside (sample 44–3) is markedly depleted.

Amphiboles in metaperidotites and metagabbro vary from calcic to calcic-sodic based on Hawthorne et al. (2012). In the former, they are classified as edenite/pargasite and richterite, whereas in the latter they plot as sadanagaite and Mg-taramite/Mg-katophorite (Fig. S5B). Rare pargasite inclusions within diopside and edenite/richterite occur in some samples (44–2, 4, 5, 6), while in the metaclinopyroxenite, pargasite is the only amphibole present and overgrows diopside. In the metagabbroic dike, the orange amphibole cores are calcic (sadanagaite), and the blue rims and overgrowths are calcic-sodic (Mg-taramite/Mg-katophorite).

Chlorite composition in banded metaperidotites, metadunites, and serpentinites have a narrow X_{Mg} range (0.90–0.96) and octahedral Al (^{O}Al in a.p.f.u.) between 0.60–1.20. Metaclinopyroxenite chlorite generally has a higher ^{O}Al than all other samples (0.80–1.20), and lower X_{Mg} (0.83–0.87). In the banded metaperidotites, compositional differences in chlorite are mainly dependent on the domain. Chlorite in olivine-rich bands occurs as spinel rims and inclusions, intergrowths with antigorite, or interstitial around olivine grains, have a higher Cr_2O_3 than chlorite from the Di-Amp-Chl bands (Fig. S6).

Antigorite is ubiquitous in all samples except for 44–10, which is serpentine-free. Late chrysotile veinlets were also identified (Fig. S7). Primary antigorite is preserved as inclusions within metamorphic olivine or diopside, whereas secondary antigorite (± magnetite) occurs as bands, veins, interstitial networks around mafic minerals, and inclusions within magnetite rims of spinel grains. Chemical analysis shows a negative trend between Si and Al compatible with Tschermak-type substitution ($Al_2Mg_{-1}Si_{-1}$) (Fig. 4E). There are no general trends between different antigorite generations. The analyzed late chrysotile veinlets have a narrow range of Si and Al (2.01–2.04 a.p.f.u. and 0.02 a.p.f.u., respectively), and higher Fe than antigorite (0.24–0.36 a.p.f.u. vs 0.12–0.22 a.p.f.u.).

Garnets are rare and only present as intergrowths with magnetite from spinel rims or single grains in samples 44–10 and 44–11. Their

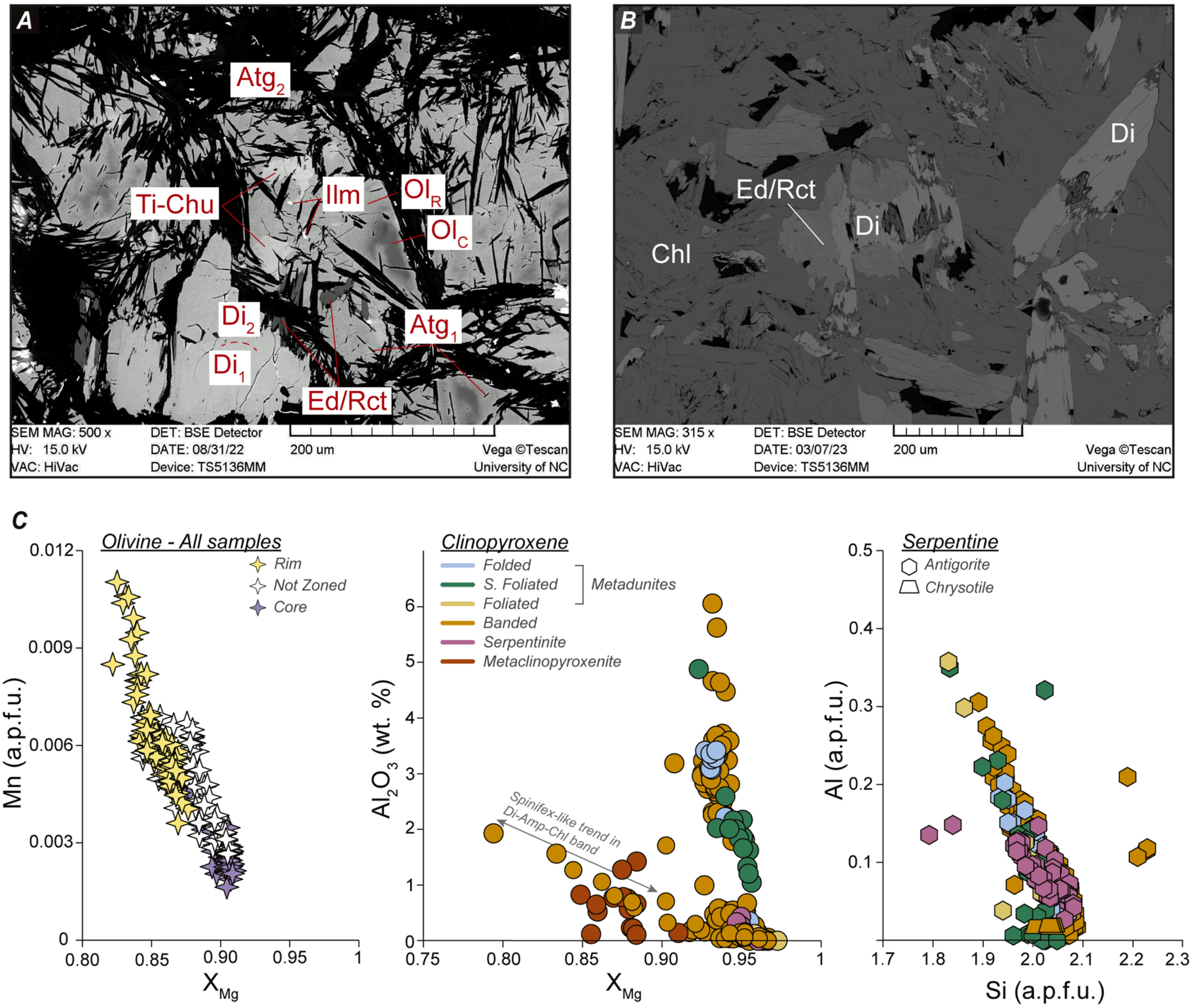

Fig. 4. Backscattered elecron images (BSE) and EMPA mineral chemistry. A. Typical mineral association of a Ti-clinohumite-bearing metaperidotites (44–2). Ol_C and Ol_R stand for olivine cores and olivine rims, respectively. B. Mineral assemblage in a Di-Amp-Chl band, where diopside cores show amphibole overgrowths in a chlorite matrix. C. Mineral chemistry data of olivine, clinopyroxene, and serpentine minerals. X_{Mg} was calculated as $X_{Mg} = Mg/(Mg+Fe^{2+})$.

chemistry is comparable to Ti-rich andradite from other subduction complexes, with TiO_2 contents between 0.1 and 9.8 wt. %. Raman spectra of garnet grains show weak to moderate OH- stretching bands in the 3550–3700 cm^{-1} region (Fig. S8).

Vesuvianite porphyroblasts chemistry is comparable to the vesuvianite found in other dikes from the quarry reported in Halama et al. (2013), albeit the TiO_2 contents in our sample are generally higher (3.5 – 6.3 wt. % vs. 0.3 – 6.4 wt. %) and no associated garnet was found (Fig. S9).

5. Geochemistry

Whole-rock chemistry compositions are given in Dataset S2. Whole-rock X_{Mg} values trend to a narrow range (0.83–0.85) except for the Di-Amp-Chl and Ol-rich band bearing samples, with values of 0.88 and 0.81, respectively. SiO_2 ranges between 42.5 and 48.0 wt. %, and the Di-Amp-Chl-band bearing sample tends to have higher CaO, Na_2O and K_2O (Fig. S10). Rare earth element (REE) data show a general depletion relative to chondrite, similar La contents, and a positive Ce anomaly (Fig. 5A-C). Contrastingly, the metagabbro has a flat, enriched REE pattern relative to the chondrite and the metaperidotites. An extended spider diagram shows similar patterns and particular enrichments in trace (e.g., Sb, As, Cs, Pb) and major elements (e.g., Na, K) relative to a depleted mantle source (Fig. 5D-F). The moderate enrichments in Na, K, and Sr are prominent only in Di-Amp-Chl bands.

5.1. In-situ Boron isotopes

Photographs of the analyzed sample mounts and the respective dataset can be found in the supplementary information appendix (Fig. S11–13) and dataset S3.

Interstitial antigorite from massive metadunites and banded metaperidotites yielded $\delta^{11}B$ values that range between −2.71 ± 1.66 ‰ and +8.78 ± 2.91 ‰. In the serpentinites, matrix antigorite displays a similar range, between −1.25 ± 2.63 ‰ and +7.04 ± 3.96 ‰, with a single outlier point of −7.68 ± 2.33 ‰. The analyzed retrograde antigorite veins have varying $\delta^{11}B$; in the metadunite 44–6, the measured vein has a narrow range between +5.73 ± 3.95 ‰ and +6.81 ± 3.29 ‰. Similarly, banded metaperidotite 44–2 has vein $\delta^{11}B$ values of +5.93 ± 1.38 ‰ and +7.68 ± 1.30 ‰. However, the antigorite vein in sample 44–3 has a broad isotopic range from −4.96 ± 1.49 ‰ to +7.29 ± 1.67 ‰ depending on the band it traverses through. An antigorite-rich band (e.g., Fig. 2G-H) yielded $\delta^{11}B$ compositions of −1.22 ± 1.49 ‰ and +2.37 ± 1.57 ‰.

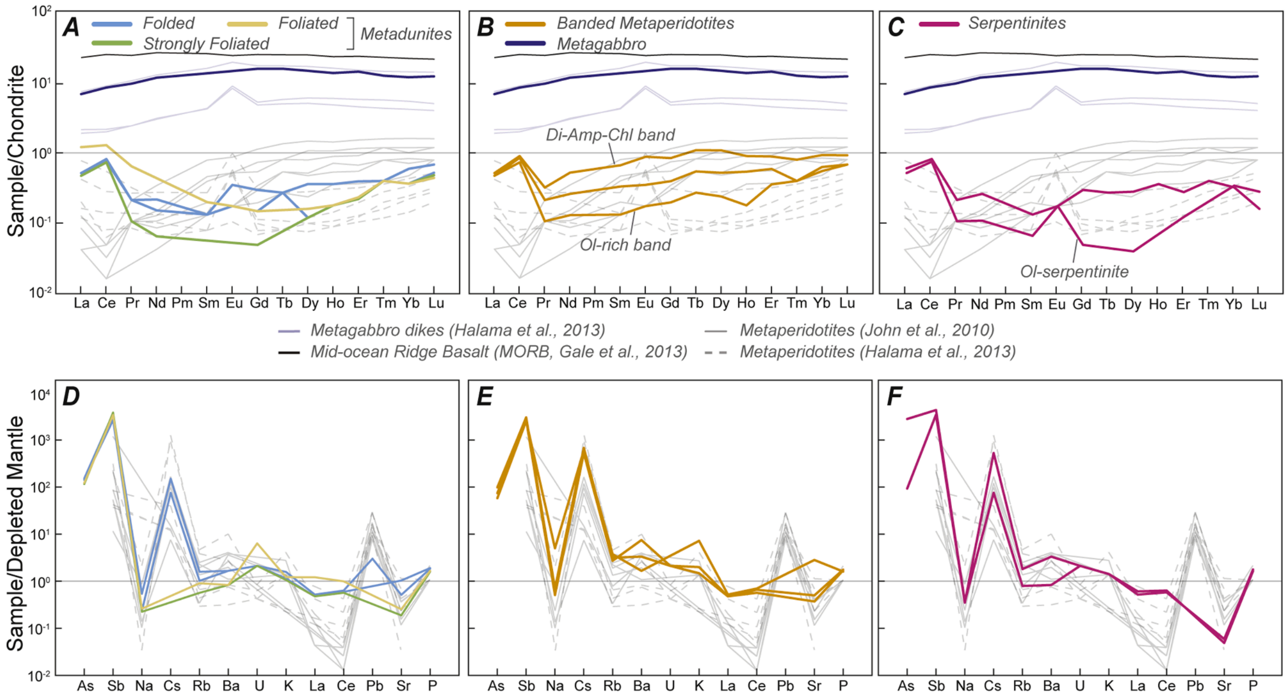

Fig. 5. Whole-rock geochemistry diagrams. A-C. Rare earth element (REE) spider diagrams normalized to chondrite after Sun and McDonough (1989). D-F. Multielement spider diagrams normalized to depleted mantle after Salters and Stracke (2004). Compiled data after Gale et al. (2013); Halama et al. (2013); and John et al. (2010).

Chlorite was measured from a spinel rim in folded metadunite 44–6 (−5.63 ± 1.76 ‰ to +5.67 ± 2.27 ‰, $n = 4$) and from the matrix of a chlorite-rich band in sample 44–3 (−5.63 ± 1.76 ‰ to +5.67 ± 2.27 ‰, $n = 2$). Pristine and rusted olivine grains from the banded metaperidotites have similar δ^{11}B, generally ranging between −3.27 ± 1.42 ‰ and +8.35 ± 2.11 ‰ ($n = 14$), and −4.12 ± 1.55 ‰ and +6.81 ± 1.67 ‰ ($n = 5$), respectively. Fine antigorite-olivine intergrowths from metadunites and banded samples have a wide δ^{11}B range from −6.55 ± 6.37 ‰ to +9.49 ± 2.83 ‰ ($n = 7$). Ti-clinohumite patches in olivine grains from metadunite 44–6 yielded values of +3.76 ± 4.34 ‰ and +6.59 ± 3.40 ‰. Amphibole from a diopside-amphibole vein in serpentinite 44–11 trend to lower values overall (−1.61 ± 3.17 ‰ to −1.42 ± 3.46 ‰).

6. Phase-equilibria modeling: thermobarometry and slab dehydration

Peak *P-T* conditions of the Raspas metaperidotites are determined based on petrological observations and phase equilibrium modeling. For instance, the absence of talc suggests minimum peak pressures of ~1.3–1.4 GPa, whereas the breakdown of Ti-clinohumite to olivine and ilmenite indicates temperatures that likely crossed the antigorite-out isograd, between ~620 and 650 °C (Fig. 4A, 7A). To further constrain the peak *P-T* conditions, we coupled our phase equilibria model with results from piston-cylinder experiments of a mixture of mineral separates commonly found in HP-UHP serpentinites (Shen et al., 2015) . In their study, the Ti-clinohumite-out and antigorite-out isograds intercept at ~1.3 GPa and ~650 °C (red lines in Fig. 7A). The offset between the antigorite-out isograds can be related to differences in the bulk composition, given that the stability of antigorite varies depending on its aluminum content (e.g., Padrón-Navarta et al., 2013). Maximum peak pressures for the metaperidotites are hypothesized to be similar to the adjacent eclogites, of 1.4–1.6 GPa, due to their spatial proximity and preserved contact between the two units (da Silva et al., 2023; Feininger, 1980). A retrograde stage is recorded in the folded metadunite by an antigorite vein, which suggests re-serpentinization temperatures between ~320–400 °C and pressures below 1.3 GPa.

Forward modeling of the metaperidotites in a H_2O-saturated system along the Raspas geothermal gradient (~13.5 °C/km) reveals that complete de-serpentinization occurs at depths of ~45–50 km. The isobaric heating stage experienced by Raspas rock assemblages does not affect the phase equilibria. For the El Toro metadunite, fluids are released in two pulses (Fig. 8A). The first pulse gradually releases ~6 wt. % of the water content at shallow depths (20–30 km) during early stages of subduction, mainly driven by the consumption of brucite and antigorite to form metamorphic olivine. At higher temperatures, an abrupt release of ~4 wt. % water results in the de-serpentinization of the rock, leading to the formation of an olivine-dominated metaharzburgite with chlorite as the main repository of the remaining water. Conversely, the chlorite-metaharzburgite only experiences a single, gradual water release pulse (~7 wt. %) associated with the simultaneous breakdown of talc and antigorite to form metamorphic olivine and orthopyroxene; in this rock, brucite is absent. The resulting mineral assemblage is dominated by orthopyroxene, contrary to the olivine-dominated assemblage in the metadunite.

For comparison, eclogites and metapelites from the La Chilca unit release discrete amounts of water (1–2 wt. % H_2O) associated with the breakdown of chlorite and chloritoid, respectively (Fig. 8C, D). The dehydration of these phases occurs at 520–580 °C and prior to complete de-serpentinization of the ultramafic rocks. Only minor pulses of water release are predicted at higher temperatures, related to partial amphibole (<1 wt. %) and white mica (<0.5 wt. %) breakdown.

7. Discussion

7.1. The exhumed record of de-serpentinization and dehydration

The recorded *P-T* conditions in the El Toro metaperidiotites and the La Chilca eclogites (Fig, 7B), and therefore the Raspas slab, indicates a warmer subduction compared to other exhumed counterparts and active subduction zones, such as Cascadia and Mexico (e.g., Syracuse et al., 2010; van Keken et al., 2018). For instance, Ti-chondrodite has been reported in metaperidotites from Tianshan (China), Zermatt-Saas (Italy), and La Cabaña (southern Chile), and its occurrence has been used as an indicator of HP-UHP conditions attained during colder subduction (González-Jiménez et al., 2017; Luoni et al., 2018; Shen et al., 2015). Ti-chondrodite becomes unstable with decreasing pressure and produces Ti-clinohumite via the reaction Ti-chondrodite + Antigorite + Olivine = Ti-clinohumite + H_2O (Shen et al., 2015). In comparison, Ti-clinohumite is found in antigorite-serpentinites and chlorite-metaharzburgites of the Betic Cordillera, which record similar *P-T* conditions as the El Toro metaperidotites (e.g., López Sánchez-Vizcaíno et al., 2005; Trommsdorff et al., 1998).

De-serpentinization of the Raspas metaperidotites, although obscured by the partial retrograde overprint, is preserved locally by the incipient breakdown of Ti-clinohumite following the reaction Ti-clinohumite = Olivine + Ilmenite + H_2O (Engi and Lindsley, 1980). In fluorine-free systems, this reaction is interpreted to be concomitant with the crossing of the antigorite-out isograd at temperatures between 620 °C and 640 °C (López Sánchez-Vizcaíno et al., 2009; Padrón-Navarta et al., 2011). Our phase equilibria model agrees with the temperature range expected for the antigorite and Ti-clinohumite breakdown, placing them at temperatures between 620 and 650 °C (Fig. 7). However, forward modeling of the metadunite (E16–44–7) cannot reproduce the observed mineralogy, which is largely dominated by metamorphic olivine (Fig. 3). The metamorphic nature of the olivine is evidenced by the occurrence of small antigorite inclusions within these grains (Fig. 4A). In addition, in a H_2O-saturated system, very little mantle-derived olivine (~4 %) is expected to be preserved at 300 °C, as the assemblage is dominated by antigorite (~80 %) and brucite (~10 %) and the increasing modal abundance of olivine is associated to the growth of metamorphic grains at the expense of brucite and antigorite (Fig. 8A). The discrepancy between the predicted versus observed mineralogy in the metadunite can be leveraged through additional forward modeling of a dunite and a harzburgite from the Oman ophiolite (Fig. S14). These models reveal that a H_2O-saturated dunite will produce an olivine-dominated ± chlorite assemblage (metadunite) after complete de-serpentinization (Fig. S14A). Similarly, a H_2O-saturated harzburgite will yield the assemblage of olivine-orthopyroxene-chlorite (chlorite-metaharzburgite) upon antigorite breakdown (Fig. S14B). This suggests that the modeled Raspas metadunite, despite the lack of other retrograde phases (diopside, amphibole, chlorite), experienced changes in its bulk composition during exhumation. The model predicts ~15 % modal metamorphic orthopyroxene after de-serpentinization albeit this phase is absent in the sample suite (Fig. 3). These changes were likely driven by extensive retrograde Si-rich metasomatism which results in the incorrect prediction of metamorphic orthopyroxene formation after de-serpentinization. On the other hand, the Raspas chlorite-metaharzburgite does agree with the textural and petrological observations reported in samples below the moho in the Raspas River (Herms et al., 2012). Therefore, while the occurrence of spinifex-texture orthopyroxene in chlorite-metaharzburgites may be an unequivocal indicator of complete de-serpentinization (e.g., Padrón-Navarta et al., 2013), metadunites dominated by metamorphic olivine also serve as

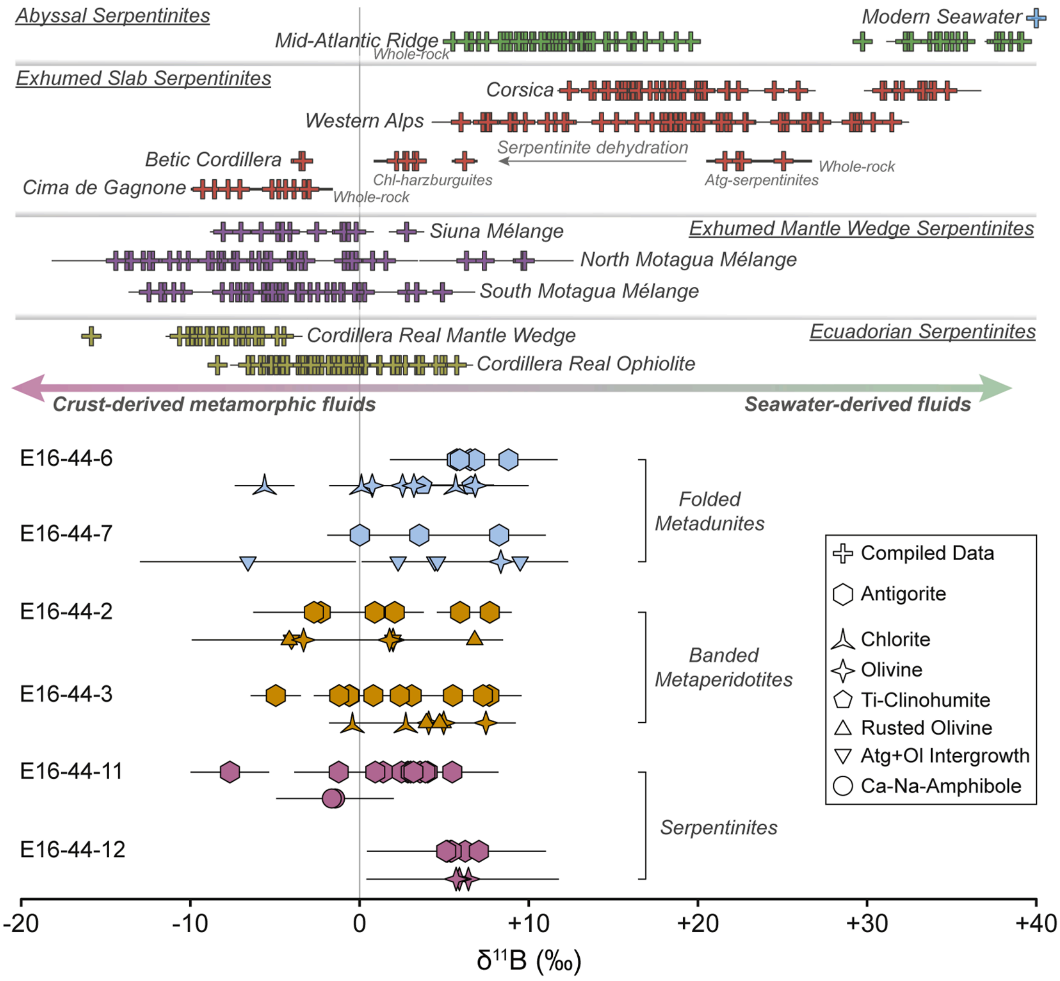

Fig. 6. B isotope data of serpentinites and associated lithologies from different tectonic and serpentinization settings, and in-situ B isotopes of the Raspas metaperidotites. Compiled data after Cannaò et al. (2015); Donoso-Tapia et al. (2024); Harvey et al. (2014); Martin et al. (2016); Martin et al. (2023); and Martin et al. (2020).

evidence of complete antigorite breakdown.

7.2. *Re-serpentinization of exhuming slab slivers*

Slab serpentinites are expected to preserve their B isotopic signature acquired during ocean floor serpentinization (~> +10 ‰; Martin et al., 2020; Vesin et al., 2024) until the antigorite-out isograd is crossed. In this critical point, a ^{11}B-rich fluid with a significantly positive δ^{11}B is released and the residual δ^{11}B of the de-serpentinized rock will trend towards lower and negative values (Cannaò et al., 2015; Harvey et al., 2014; Martin et al., 2016). In the El Toro metaperidotites, the boron isotopic signature is akin to serpentinization by subducted crust-derived metamorphic fluids (Fig. 6), overlapping the ranges of chlorite-harzburguites from the Betic Cordillera and ophiolitic serpentinites from the Cordillera Real (Donoso-Tapia et al., 2024; Harvey et al., 2014). In this scenario, the re-serpentinization of the metaperidotites likely erased the original seawater-derived signature typical of slab serpentinites (Martin et al., 2020). Moreover, the observed differences in serpentine textures (e.g., interstitial porosity network, veins, matrix antigorite) and the extent of serpentinization (e.g., partial and fully serpentinized samples) suggest that the fluid infiltration occurred as pervasive and channelized events at temperatures between 320 and 400 °C, indicated by aluminum in antigorite isopleths from a retrograde vein (Fig. 7A).

The boron isotopic signature is expected to behave differently depending on the fluid infiltration style (e.g., channelized vs. pervasive), displaying either homogeneous or heterogeneous δ^{11}B values throughout the different microtextures in a sample depending on the relative fluid/rock ratio (Evans et al., 2024; Martin et al., 2023). Homogeneity in our sample suite is particularly notable in the metadunite 44–6 and serpentinite 44–12, where the $\delta^{11}B_{Atg}$ values vary between ~2–3 ‰. The dense vein-veinlet network observed in the metadunite may attest that a mainly channelized fluid under high fluid/rock ratios also facilitates isotopic homogeneity, something usually expected for serpentinization by a pervasive fluid (Martin et al., 2023). In comparison, wider $\delta^{11}B_{Atg}$ ranges compatible with heterogeneous isotopic signatures are recorded in veins and veinlets of the banded metaperidotites 44–2 and 44–3, in which there is a difference of up to ~10 ‰ between the center of the veinlet and interstitial antigorite away (~1 mm) from the vein, and an along-vein $\delta^{11}B_{Atg}$ variation of ~12 ‰, respectively. This strongly suggests that the channelized fluids responsible for these veins/veinlets infiltrated at fluid/rock ratios low enough to prevent isotopic homogenization. In summary, the observed isotopic homogeneity allows to constrain the boron isotopic signature of the fluid responsible for re-serpentinizing the metaperidotites, ranging from ~−6 to +8 ‰ and compatible with metamorphic fluids derived from subducting crust.

Along with the re-serpentinization of the metaperidotites, the strong metasomatic overprint is also evidenced by the development of diopside-amphibole-chlorite bands and amphibole overgrowths around diopside and olivine (Fig. 2E, 2G, & 4B). The contrasting modal proportion and style of occurrence of these phases in massive metadunites and banded metaperidotites indicate that fluid circulation was facilitated and likely controlled by interconnected porosity networks (e.g., Huber et al., 2022), hydraulic fracturing (i.e., veins and veinlets), and pre-existing mantle layering (Fig. 3). In the latter case, the association of rusted olivine near the edge of the olivine-rich bands and antigorite-rich bands may be direct evidence of channelized flow along a pre-existing discontinuity that acted as a pathway, in this case, the contact between the olivine and pyroxene-rich layers. Similarly, the resulting Di-Amp-Chl bands are metasomatic products of relic augite alteration and recrystallization under varying fluid-rock ratios, this explains the well-preserved pseudo-spinifex diopside grains versus the amorphous diopside cores overgrown by edenite/richterite (Fig. 4B).

7.3. *The Raspas paleo-subduction zone: a window into shallow slab dehydration and fluid circulation*

Previous studies on the Raspas Complex have sparked a debate concerning its origin, either relating it to a subducted seamount (e.g.,

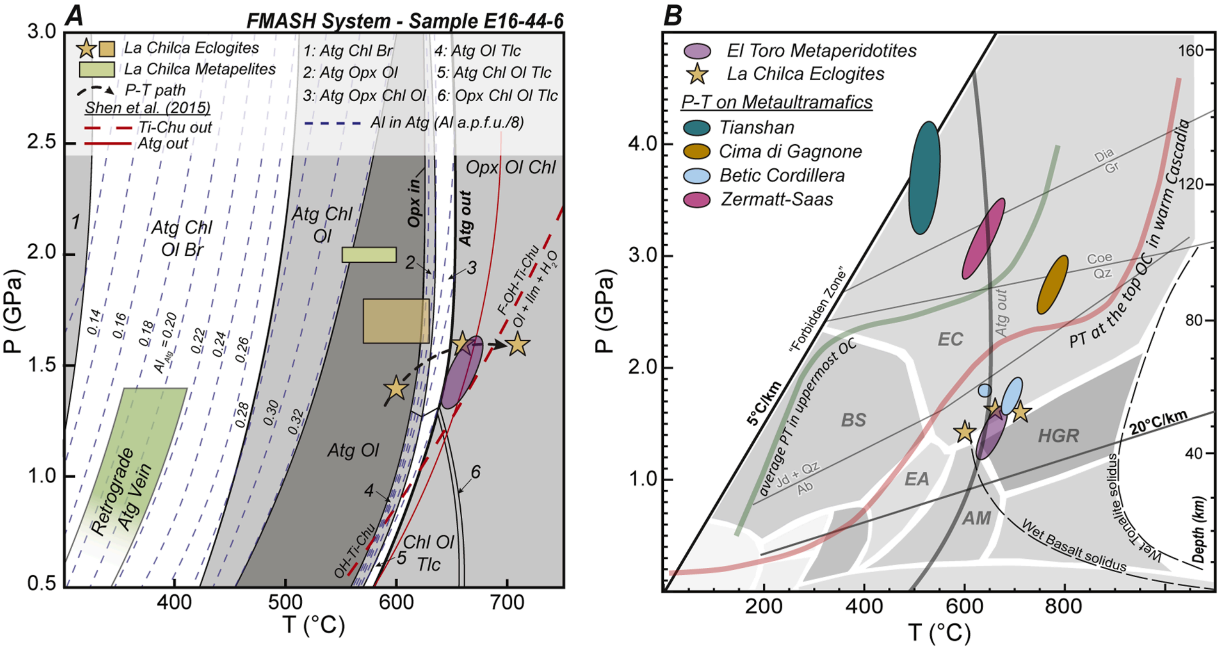

Fig. 7. *P-T* diagrams of the Raspas Complex and other subduction complexes worldwide where de-serpentinization has been reported. A. *P-T* phase diagram for metadunite E16–44–6. The purple oval represents the calculated peak *P-T* conditions for the El Toro unit, and the green field is the temperature range for a retrograde vein in the same sample. Green and brown rectangles are *P-T* data from Gabriele et al. (2003) and John et al. (2010) for eclogite-facies metasediments and metabasites, respectively. Brown stars represent the three stages of the path recorded on the La Chilca eclogites after da Silva et al. (2023). B. Compiled *P-T* conditions of other subduction complexes worldwide (see the main text). For reference, the *P-T* also show the average *P-T* path followed by the uppermost oceanic crust (OC) as well as the *P-T* path for Cascadia (van Keken et al., 2018).

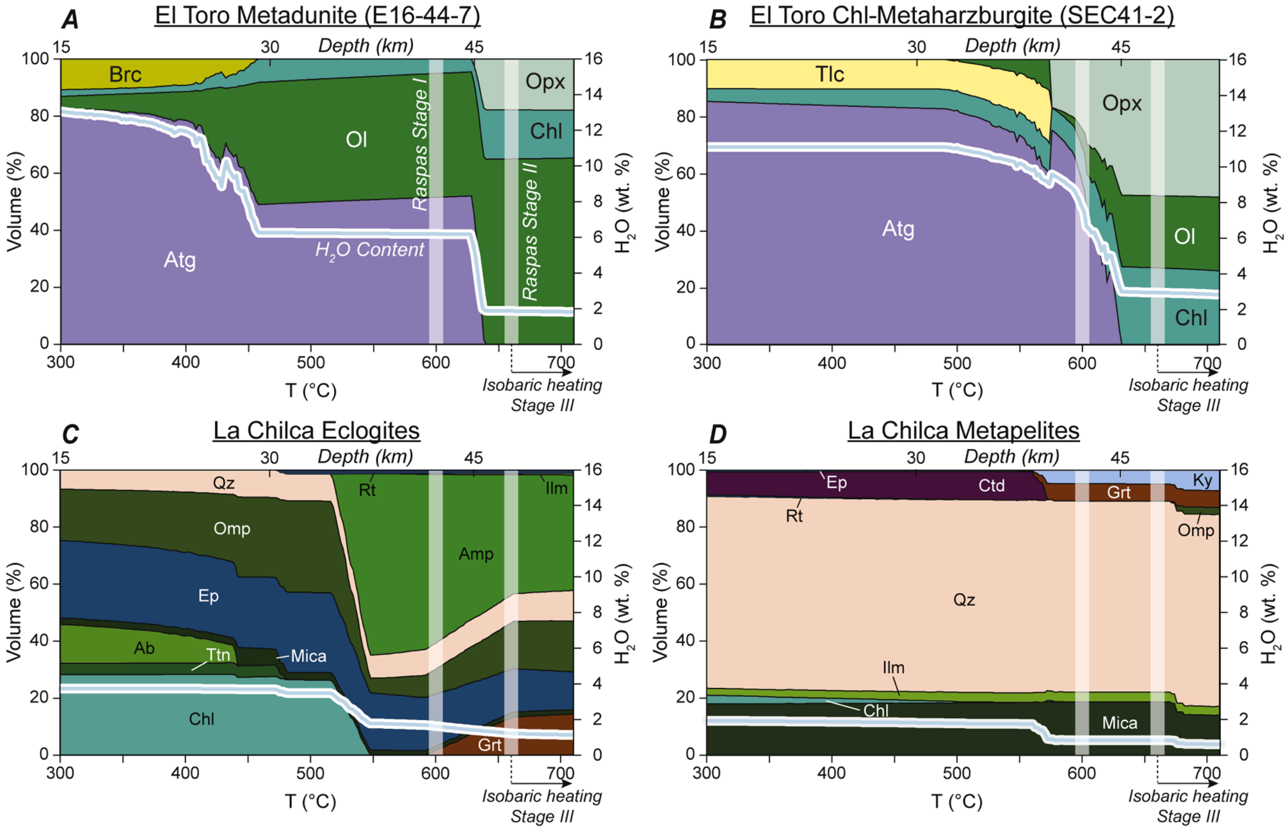

Fig. 8. Phase assemblage evolution of representative lithologies of the Raspas Complex during warm subduction (Gabriele et al., 2003; Herms et al., 2012; John et al., 2010). The translucent white bars represent stages I and II recorded in Raspas eclogites. Thermal gradient used for these calculations is from da Silva et al. (2023).

John et al., 2010) or a subducted oceanic plateau (e.g., Arculus et al., 1999; da Silva et al., 2023). Regardless of its origin, numerical models simulating the subduction of such asperities and thickened oceanic crust predict an impact on the stress distribution along the slab and overriding plate, and in some cases, it can lead to the exhumation of HP-UHP terranes (Ruh et al., 2016; Vogt and Gerya, 2014). The subduction of an oceanic plateau is capable of triggering flat-slab segments where the thickened portion of the crust interacts with the overlying hot asthenosphere, leading to a warmer geotherm (e.g., van Hunen et al., 2002). This implies that the de-serpentinization of the oceanic mantle can be achieved at shallower depths than expected, between 70 and 150 km (e.g., Reynard, 2013). Additionally, recent models of an evolving subduction zone show that during early and intermediate stages of subduction, slab dehydration, including de-serpentinization, occurs at shallower levels when compared to mature subduction stages as a consequence of a dynamic thermal structure (Epstein et al., 2024). In this scenario, the subduction of an anomalous, thickened oceanic crust may have driven the thermal gradient to higher values. Based on their model, the duration of this warmer gradient was likely not prolonged, given that after ~30 Ma, the subduction system is expected to be mature enough to trigger de-serpentinization at deeper depths (~80 km).

Forward modeling integrating the Raspas slab lithologies reveals that the subducted serpentinized mantle dominates the water released compared to the crustal sections (Fig. 9A, B). Nonetheless, fluid circulation along the Raspas paleo-subduction zone was already active at depths of 25–45 km, and complete de-serpentinization at ~50 km further enhanced the fluid flow along the slab and overlying mantle wedge. This may explain the mixed fluid signatures that affected the MORB- and zoisite-eclogites, which have been interpreted as being sourced from dehydrating metabasites, metasediments, and serpentinites (e.g., Halama et al., 2011; Herms et al., 2012). Our models for all lithologies agree with other fluid release calculations for different subduction zones (Hernández-Uribe and Palin, 2019; Smye and England, 2023). The depth range of metamorphic-driven dehydration in the Raspas paleo-subduction system is compatible with the occurrence of non-volcanic tremors (NVT) and slow-slip events (SSE) at depths of ~25–65 km in warm active subduction zones worldwide (Condit et al., 2020; Gutiérrez-Aguilar et al., 2022; Hernández-Uribe and Gutiérrez-Aguilar, 2021). However, this depth range is commonly associated to the dehydration of metabasites and metapelites, while hydrated peridotites are not expected to contribute significantly (Condit et al., 2020). Thus, the Raspas paleo-subduction system records a particularly warm environment where de-serpentinization enhanced an already active fluid circulation network.

During exhumation, the Raspas slab sliver interacted with fluids that triggered the re-serpentinization of the metaperidotites (Fig. 9C). The measured boron isotopes in the metaperidotites reveal that the re-serpentinization was driven by slab-derived crustal fluids, similar to subduction interface- and mantle wedge-derived serpentinites from Central America and the Ecuadorian Cordillera Real (Donoso-Tapia et al., 2024; Martin et al., 2016). These Si-Ca-Na-K-rich fluids were also responsible for promoting the development of Di-Amp-Chl bands through pre-existing discontinuities and/or foliation that acted as fluid pathways, similar to jadeitite-forming fluids (e.g., Angiboust et al., 2021; Harlow et al., 2016). The associated amphibole-vesuvianite dikes and overlying eclogites and blueschists were similarly affected during exhumation, revealed by the strong peaks in K and P, and moderate peaks in Ba (Fig. 9D). In the metaperidotites, enrichments in Na, K, Ba, and Sr are nearly exclusive to the Di-Amp-Chl bands, confirming that these bands effectively served as fluid channels (Fig. 9E). Thus, the ascending Raspas slab sliver encountered metamorphic fluids sourced from the upper portion of the underlying subducting crust. Common

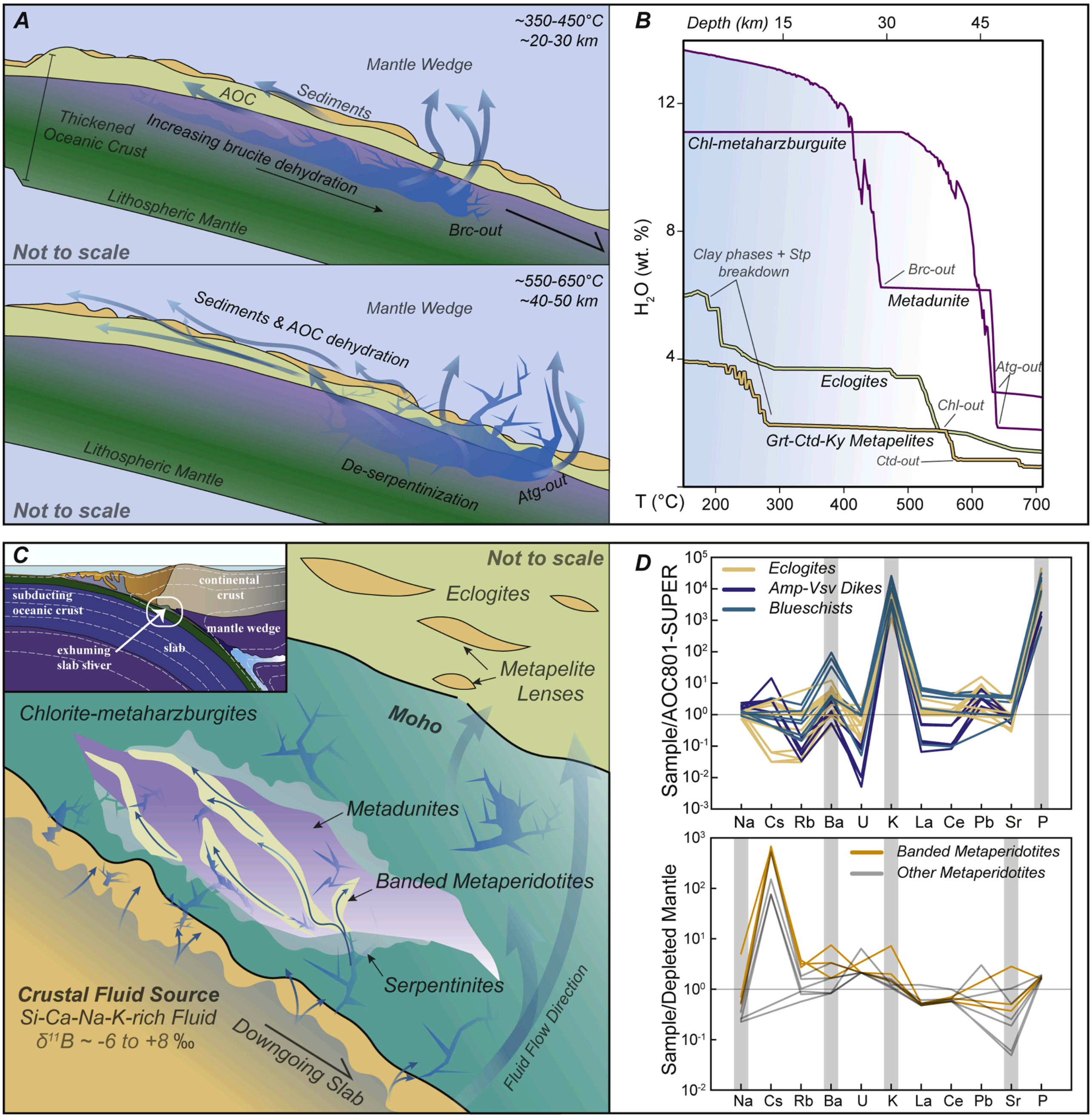

Fig. 9. Summary of the metamorphic history of the Raspas slab. A. Cartoon of the prograde path showing key layers and dehydration reactions. B. Evolution of the water content stored in the lithologies found in the Raspas Complex along the estimated geothermal gradient by da Silva et al. (2023). C. Cartoon of the retrograde path showing key fluid circulation features. D. Spider diagram of eclogites, dikes, and blueschists from the La Chilca unit; and of the metaperidotites from this study. Geodynamic model in C is after Vogt and Gerya (2014).

peaks in K, Ba, and Cs found in eclogites/blueschists and metaperidotites suggest that both layers were affected by similar fluids. Peaks in As, Sb and Pb in the metaperidotites further suggest that re-serpentinization was driven by fluids derived from a slab, crustal source. While both sediment- and seawater-derived fluids are capable of producing such enrichments, the B isotope data suggest a negligible influence of seawater, similar to serpentinites in the Cordillera Real of Ecuador (Donoso-Tapia et al., 2024; Peters et al., 2017).

Further infiltration of fluids at shallow crustal levels and low temperatures is evidenced by discrete veinlets of chrysotile ± magnesite, mainly present in the banded metaperidotites. However, the general scarcity of carbonate phases suggests that the circulating fluids were CO_2-poor.

8. Conclusions

Metaperidotites of the El Toro unit in the Raspas Complex preserve evidence of total de-serpentinization after reaching peak *P-T* conditions of 1.3–1.6 GPa and ~620–650 °C, based on the observed breakdown of Ti-clinohumite to metamorphic olivine and ilmenite, which suggests the crossing of the antigorite-out isograd. During exhumation, crust-derived metamorphic fluids heavily metasomatized the metaperidotites through pervasive and channelized fluid infiltration episodes under varying fluid/rock ratios, triggering their re-serpentinization at shallower crustal levels (<1.3 GPa, 320–400 °C). The circulating fluids were likely Si-Ca-Na-K-rich and affected the overlying eclogites and blueschists from the La Chilca unit, as indicated by common enrichments in these and other trace elements. Forward modeling of the Raspas slab reveals that de-serpentinization of the subducted oceanic mantle is the primary source of fluids at depths of ~50 km, while fluid circulation at shallower levels (~25–45 km) is mainly controlled by brucite breakdown and dehydration of chlorite and chloritoid from the crustal sections. This range overlaps with depths of non-volcanic tremors and slow-slip events observed in warm active subduction zones worldwide. Thus, the Raspas Complex offers an *in-situ* window into the fluids responsible for triggering these seismic events.

CRediT authorship contribution statement

Damián Donoso-Tapia: Writing – review & editing, Writing – original draft, Visualization, Validation, Software, Methodology, Investigation, Formal analysis, Data curation, Conceptualization. **Kennet E. Flores:** Writing – review & editing, Visualization, Validation, Supervision, Resources, Project administration, Methodology, Investigation, Funding acquisition, Formal analysis, Data curation, Conceptualization. **Celine Martin:** Writing – review & editing, Validation, Resources, Project administration, Methodology, Investigation, Funding acquisition, Formal analysis, Data curation, Conceptualization. **Sarah Hull:** Writing – review & editing, Validation, Software, Methodology, Investigation, Formal analysis, Data curation. **David Hernández-Uribe:** Writing – review & editing, Software, Methodology, Formal analysis, Data curation. **Esteban Gazel:** Writing – review & editing, Validation, Resources, Formal analysis, Data curation.

Declaration of competing interest

The authors declare that they have no known competing financial interests or personal relationships that could have appeared to influence the work reported in this paper.

Acknowledgments

This study was supported by the US National Science Foundation EAR 2150618 to K.E.F and EAR 1951166 to C.M. The authors thank the helpful assistance of Jeffrey Marsh (Laurentian University) for assisting in the sample collection and field logistics, Kyle Dayton (Cornell), Lyndsey Fisher (Cornell), and Louise Bolge (LDEO), with the Raman, LA-ICP-MS, and LA-MC-ICP-MS facilities, respectively. DDT thanks Clément Herviou (UNC), Xiaoming Liu (UNC), Drew Coleman (UNC), Jesse Walters (University of Graz, Austria), and George E. Harlow (AMNH) for their valuable discussion and input. We are grateful for insightful suggestions from anonymous reviewers that enhanced the manuscript.

Supplementary materials

Supplementary material associated with this article can be found, in the online version, at doi:10.1016/j.epsl.2025.119213.

Data availability

Data is included in supplementary materials and shared on EarthChem

References

Ague, J.J., Tassara, S., Holycross, M.E., Li, J.-L., Cottrell, E., Schwarzenbach, E.M., Fassoulas, C., John, T., 2022. Slab-derived devolatilization fluids oxidized by subducted metasedimentary rocks. Nat. Geosci. 15, 320–326. https://doi.org/10.1038/s41561-022-00904-7.

Angiboust, S., Agard, P., Jolivet, L., Beyssac, O., 2009. The Zermatt-Saas ophiolite: the largest (60-km wide) and deepest (c. 70–80 km) continuous slice of oceanic lithosphere detached from a subduction zone? Terra Nova 21, 171–180. https://doi.org/10.1111/j.1365-3121.2009.00870.x.

Angiboust, S., Glodny, J., Cambeses, A., Raimondo, T., Monié, P., Popov, M., Garcia-Casco, A., 2021. Drainage of subduction interface fluids into the forearc mantle evidenced by a pristine jadeitite network (Polar Urals). J. Metamorph. Geol. 39, 473–500. https://doi.org/10.1111/jmg.12570.

Arculus, R.J., Lapierre, H., Jaillard, E., 1999. Geochemical window into subduction and accretion processes: raspas metamorphic complex. Ecuador. Geol. 27, 547–550. https://doi.org/10.1130/0091-7613(1999)027<0547:GWISAA>2.3.CO;2.

Aspden, J.A., Bonilla, W., Duque, P., 1995. The El Oro metamorphic complex, Ecuador: geology and economic mineral deposits. British Geol. Surv.

Bellido, F., Valverde, P., Jaimes, F., Carlotto, V., Díaz-Martinez, E., 2009. Datación y caracterización geoquímica de los granitoides peralumínicos de los cerros de Amotape y de los Macizos de Illescas y Paita (Noroeste de Perú). Boletín de la Sociedad Geológica del Perú 103, 197–213.

Bosch, D., Gabriele, P., Lapierre, H., Malfere, J.-L., Jaillard, E., 2002. Geodynamic significance of the Raspas metamorphic Complex (SW Ecuador): geochemical and isotopic constraints. Tectonophysics 345, 83–102. https://doi.org/10.1016/S0040-1951(01)00207-4.

Cannaò, E., Agostini, S., Scambelluri, M., Tonarini, S., Godard, M., 2015. B, Sr and Pb isotope geochemistry of high-pressure Alpine metaperidotites monitors fluid-mediated element recycling during serpentinite dehydration in subduction mélange (Cima di Gagnone, Swiss Central Alps). Geochim. Cosmochim. Acta 163, 80–100. https://doi.org/10.1016/j.gca.2015.04.024.

Condit, C.B., Guevara, V.E., Delph, J.R., French, M.E., 2020. Slab dehydration in warm subduction zones at depths of episodic slip and tremor. Earth. Planet. Sci. Lett. 552, 116601. https://doi.org/10.1016/j.epsl.2020.116601.

Connolly, J.A.D., 2005. Computation of phase equilibria by linear programming: a tool for geodynamic modeling and its application to subduction zone decarbonation. Earth. Planet. Sci. Lett. 236, 524–541. https://doi.org/10.1016/j.epsl.2005.04.033.

da Silva, S., Bustamante, A., Bustamante, C., Cardona, A., Juliani, C., 2023. Early Cretaceous subduction of an oceanic plateau at the Northern Andes; geochemical, metamorphic, and cooling age constraints of the Raspas metamorphic Complex. Lithos. 456-457, 107299. https://doi.org/10.1016/j.lithos.2023.107299.

Donoso-Tapia, D., Flores, K.E., Martin, C., Gazel, E., Marsh, J., 2024. Exhumed serpentinites and their tectonic significance in non-collisional orogens. Geochem., Geophys., Geosys. 25, e2023GC011072. https://doi.org/10.1029/2023GC011072.

Donoso-Tapia, D., Flores, K.E., Martin, C., Hull, S., Hernández-Uribe, D., Gazel, E., 2025a. In-situ Boron isotopes (δ11B) Measured By LA-MC-ICP-MS of Raspas Complex, Version 1.0, in: (IEDA). EarthChem. I.E.D.A. (Ed.).

Donoso-Tapia, D., Flores, K.E., Martin, C., Hull, S., Hernández-Uribe, D., Gazel, E., 2025b. Raspas Complex minerals EMPA data, Version 1.0, in: (IEDA). EarthChem. I.E.D.A. (Ed.).

Donoso-Tapia, D., Flores, K.E., Martin, C., Hull, S., Hernández-Uribe, D., Gazel, E., 2025c. Whole-rock Major (XRF) and Trace Element (LA-ICP-MS) Data of Raspas Complex, Version 1.0, in: (IEDA). EarthChem. I.E.D.A. (Ed.).

Egüez, A., Gaona, M., 2017. Mapa Geologico de la Republica del Ecuador 2017.

Engi, M., Lindsley, D.H., 1980. Stability of titanian clinohumite: experiments and thermodynamic analysis. Contrib. Mineral. Petrol. 72, 415–424. https://doi.org/10.1007/BF00371348.

Epstein, G.S., Condit, C.B., Stoner, R.K., Holt, A.F., Guevara, V.E., 2024. Evolving subduction zone thermal structure drives extensive forearc mantle wedge hydration. AGU Adv. 5, e2023AV001121. https://doi.org/10.1029/2023AV001121.

Evans, A.D., Standish, C.D., Milton, J.A., Robbins, A.G., Craw, D., Foster, G.L., Teagle, D.A.H., 2024. Imaging of boron in altered mantle rocks illuminates progressive serpentinisation episodes. Geochem. Perspect. Lett. 29, 20–25.

Evans, K.A., Powell, R., Frost, B.R., 2013. Using equilibrium thermodynamics in the study of metasomatic alteration, illustrated by an application to serpentinites. Lithos. 168-169, 67–84. https://doi.org/10.1016/j.lithos.2013.01.016.

Feininger, T., 1980. Eclogite and related high-pressure regional metamorphic rocks from the andes of ecuador*. J. Petrol. 21, 107–140. https://doi.org/10.1093/petrology/21.1.107.

Gabriele, P., 2002. HP Terranes exhumation in an active margin setting: geology, petrology and geochemistry of the Raspas compex in SW Ecuador.

Gabriele, P., Ballèvre, M., Jaillard, E., Hernandez, J., 2003. Garnet-chloritoid-kyanite metapelites from the Raspas Complex (SW Ecuador): a key eclogite-facies assemblage. Eur. J. Mineral. 15, 977–990.

Gale, A., Dalton, C.A., Langmuir, C.H., Su, Y., Schilling, J.-G., 2013. The mean composition of ocean ridge basalts. Geochem., Geophys., Geosys. 14, 489–518. https://doi.org/10.1029/2012GC004334.

González-Jiménez, J.M., Plissart, G., Garrido, L.N., Padrón-Navarta, J.A., Aiglsperger, T., Romero, R., Marchesi, C., Moreno-Abril, A.J., Reich, M., Barra, F., Morata, D., 2017. Titanian clinohumite and chondrodite in antigorite serpentinites from Central Chile: evidence for deep and cold subduction. Eur. J. Mineral. 29, 959–970. https://doi.org/10.1127/ejm/2017/0029-2668.

Gutiérrez-Aguilar, F., Hernández-Uribe, D., Holder, R.M., Condit, C.B., 2022. Fluid-induced fault reactivation due to Brucite + Antigorite dehydration triggered the Mw7.1 September 19th Puebla-Morelos (Mexico) intermediate-depth earthquake. Geophys. Res. Lett. 49, e2022GL100814. https://doi.org/10.1029/2022GL100814.

Halama, R., Bebout, G.E., John, T., Schenk, V., 2010. Nitrogen recycling in subducted oceanic lithosphere: the record in high- and ultrahigh-pressure metabasaltic rocks. Geochim. Cosmochim. Acta 74, 1636–1652. https://doi.org/10.1016/j.gca.2009.12.003.

Halama, R., John, T., Herms, P., Hauff, F., Schenk, V., 2011. A stable (Li, O) and radiogenic (Sr, Nd) isotope perspective on metasomatic processes in a subducting slab. Chem. Geol. 281, 151–166. https://doi.org/10.1016/j.chemgeo.2010.12.001.

Halama, R., Savov, I.P., Garbe-Schönberg, D., Schenk, V., Toulkeridis, T., 2013. Vesuvianite in high-pressure-metamorphosed oceanic lithosphere (Raspas Complex, Ecuador) and its role for transport of water and trace elements in subduction zones. Eur. J. Mineral. 25, 193–219.

Harlow, G.E., Flores, K.E., Marschall, H.R., 2016. Fluid-mediated mass transfer from a paleosubduction channel to its mantle wedge: evidence from jadeitite and related rocks from the Guatemala Suture Zone. Lithos. 258-259, 15–36. https://doi.org/10.1016/j.lithos.2016.04.010.

Harvey, J., Garrido, C.J., Savov, I., Agostini, S., Padrón-Navarta, J.A., Marchesi, C., López Sánchez-Vizcaíno, V., Gómez-Pugnaire, M.T., 2014. 11B-rich fluids in subduction zones: the role of antigorite dehydration in subducting slabs and boron isotope heterogeneity in the mantle. Chem. Geol. 376, 20–30. https://doi.org/10.1016/j.chemgeo.2014.03.015.

Hawthorne, F.C., Oberti, R., Harlow, G.E., Maresch, W.V., Martin, R.F., Schumacher, J. C., Welch, M.D., 2012. Nomenclature of the amphibole supergroup. Am. Mineral. 97, 2031–2048. https://doi.org/10.2138/am.2012.4276.

Herms, P., John, T., Bakker, R.J., Schenk, V., 2012. Evidence for channelized external fluid flow and element transfer in subducting slabs (Raspas Complex, Ecuador). Chem. Geol. 310-311, 79–96. https://doi.org/10.1016/j.chemgeo.2012.03.023.

Hernández-Uribe, D., Gutiérrez-Aguilar, F., 2021. The versatility of petrological modeling: thermobarometry of high-pressure metabasites from the Renge and Sanbagawa belts and phase evolution during warm subduction at Nankai. Island Arc. 30, e12406. https://doi.org/10.1111/iar.12406.

Hernández-Uribe, D., Palin, R.M., 2019. A revised petrological model for subducted oceanic crust: insights from phase equilibrium modelling. J. Metamorph. Geol. 37, 745–768. https://doi.org/10.1111/jmg.12483.

Huber, K., Vrijmoed, J.C., John, T., 2022. Formation of olivine veins by reactive fluid flow in a dehydrating serpentinite. Geochemistry, Geophysics, Geosystems. https://doi.org/10.1029/2021GC010267, 23, e2021GC010267.

INGEMMET, 2022. Mapa Geologico de Peru 1:1000000. In: Regional, D.d.G. (Ed.), Insituto Geológico Minero y Metalúrgico. Lima, Peru.

John, T., Scherer, E.E., Schenk, V., Herms, P., Halama, R., Garbe-Schönberg, D., 2010. Subducted seamounts in an eclogite-facies ophiolite sequence: the Andean Raspas complex. SW Ecuador. Contrib. Mineral. Petrol. 159, 265–284. https://doi.org/10.1007/s00410-009-0427-0.

Kempf, E.D., Hermann, J., Reusser, E., Baumgartner, L.P., Lanari, P., 2020. The role of the antigorite + brucite to olivine reaction in subducted serpentinites (Zermatt, Switzerland). Swiss. J. Geosci. 113, 16. https://doi.org/10.1186/s00015-020-00368-0.

Litherland, M., 1994. The metamorphic belts of ecuador. British Geolog. Surv, Overseas Memoir 11.

López Sánchez-Vizcaíno, V., Gómez-Pugnaire, M.T., Garrido, C.J., Padrón-Navarta, J.A., Mellini, M., 2009. Breakdown mechanisms of titanclinohumite in antigorite serpentinite (Cerro del Almirez massif, S. Spain): a petrological and TEM study. Lithos. 107, 216–226. https://doi.org/10.1016/j.lithos.2008.10.008.

López Sánchez-Vizcaíno, V., Trommsdorff, V., Gómez-Pugnaire, M.T., Garrido, C.J., Müntener, O., Connolly, J.A.D., 2005. Petrology of titanian clinohumite and olivine at the high-pressure breakdown of antigorite serpentinite to chlorite harzburgite (Almirez Massif, S. Spain). Contrib. Mineral. Petrol. 149, 627–646. https://doi.org/10.1007/s00410-005-0678-3.

Luoni, P., Rebay, G., Spalla, M.I., Zanoni, D., 2018. UHP Ti-chondrodite in the Zermatt-Saas serpentinite: constraints on a new tectonic scenario. 103, 1002–1005, doi:10.2138/am-2018-6460.

Martin, C., Flores, K.E., Harlow, G.E., 2016. Boron isotopic discrimination for subduction-related serpentinites. Geology. 44, 899–902. https://doi.org/10.1130/G38102.1.

Martin, C., Flores, K.E., Harlow, G.E., Angiboust, S., Hodel, F., Guice, G.L., 2023. The B isotopic signature of serpentine from obducted ophiolites: mixing of fluids and tectonic implications. Lithos. 456-457, 107275. https://doi.org/10.1016/j.lithos.2023.107275.

Martin, C., Flores, K.E., Vitale-Brovarone, A., Angiboust, S., Harlow, G.E., 2020. Deep mantle serpentinization in subduction zones: insight from in situ B isotopes in slab and mantle wedge serpentinites. Chem. Geol. 545, 119637. https://doi.org/10.1016/j.chemgeo.2020.119637.

Martin, C., Ponzevera, E., Harlow, G., 2015. In situ lithium and boron isotope determinations in mica, pyroxene, and serpentine by LA-MC-ICP-MS. Chem. Geol. 412, 107–116. https://doi.org/10.1016/j.chemgeo.2015.07.022.

Morimoto, N., 1988. Nomenclature of Pyroxenes. Mineral. Petrol. 39, 55–76. https://doi.org/10.1007/BF01226262.

Mourier, T., Laj, C., Mégard, F., Roperch, P., Mitouard, P., Farfan Medrano, A., 1988. An accreted continental terrane in northwestern Peru. Earth. Planet. Sci. Lett. 88, 182–192. https://doi.org/10.1016/0012-821X(88)90056-8.

Padrón-Navarta, J.A., López Sánchez-Vizcaíno, V., Garrido, C.J., Gómez-Pugnaire, M.T., 2011. Metamorphic record of high-pressure dehydration of antigorite serpentinite to chlorite harzburgite in a subduction setting (Cerro del Almirez, Nevado–Filábride Complex, Southern Spain). J. Petrol. 52, 2047–2078. https://doi.org/10.1093/petrology/egr039.

Padrón-Navarta, J.A., Sánchez-Vizcaíno, V.L., Hermann, J., Connolly, J.A.D., Garrido, C. J., Gómez-Pugnaire, M.T., Marchesi, C., 2013. Tschermak's substitution in antigorite and consequences for phase relations and water liberation in high-grade serpentinites. Lithos. 178, 186–196. https://doi.org/10.1016/j.lithos.2013.02.001.

Peters, D., Bretscher, A., John, T., Scambelluri, M., Pettke, T., 2017. Fluid-mobile elements in serpentinites: constraints on serpentinisation environments and element cycling in subduction zones. Chem. Geol. 466, 654–666. https://doi.org/10.1016/j.chemgeo.2017.07.017.

Piccoli, F., Hermann, J., Pettke, T., Connolly, J.A.D., Kempf, E.D., Vieira Duarte, J.F., 2019. Subducting serpentinites release reduced, not oxidized, aqueous fluids. Sci. Rep. 9, 19573. https://doi.org/10.1038/s41598-019-55944-8.

Reynard, B., 2013. Serpentine in active subduction zones. Lithos. 178, 171–185. https://doi.org/10.1016/j.lithos.2012.10.012.

Ruh, J.B., Sallarès, V., Ranero, C.R., Gerya, T., 2016. Crustal deformation dynamics and stress evolution during seamount subduction: high-resolution 3-D numerical modeling. J. Geophys. Res.: Solid Earth 121, 6880–6902. https://doi.org/10.1002/2016JB013250.

Salters, V.J.M., Stracke, A., 2004. Composition of the depleted mantle. Geochem., Geophys., Geosys. 5. https://doi.org/10.1029/2003GC000597.

Scambelluri, M., Pettke, T., Rampone, E., Godard, M., Reusser, E., 2014. Petrology and trace element budgets of high-pressure peridotites indicate subduction dehydration of serpentinized mantle (Cima di Gagnone, Central Alps, Switzerland). J. Petrol. 55, 459–498. https://doi.org/10.1093/petrology/egt068.

Shen, T., Hermann, J., Zhang, L., Lü, Z., Padrón-Navarta, J.A., Xia, B., Bader, T., 2015. UHP metamorphism documented in Ti-chondrodite- and Ti-clinohumite-bearing serpentinized ultramafic rocks from Chinese Southwestern Tianshan. J. Petrol. 56, 1425–1458. https://doi.org/10.1093/petrology/egv042.

Smye, A.J., England, P.C., 2023. Metamorphism and deformation on subduction interfaces: 2. Petrological and tectonic implications. Geochem., Geophy., Geosys. 24, e2022GC010645. https://doi.org/10.1029/2022GC010645.

Sun, S.s., McDonough, W.F., 1989. Chemical and isotopic systematics of oceanic basalts: implications for mantle composition and processes. Geological Society, London, Special Publications 42, 313–345, 10.1144/GSL.SP.1989.042.01.19.

Syracuse, E.M., van Keken, P.E., Abers, G.A., 2010. The global range of subduction zone thermal models. Phy. Earth Planet. Inter. 183, 73–90. https://doi.org/10.1016/j.pepi.2010.02.004.

Trommsdorff, V., Sánchez-Vizcaíno, V.L., Gómez-Pugnaire, M.T., Müntener, O., 1998. High pressure breakdown of antigorite to spinifex-textured olivine and orthopyroxene. SE Spain. Contrib. Mineral. Petrol. 132, 139–148. https://doi.org/10.1007/s004100050412.

Ulrich, M., Rubatto, D., Hermann, J., Markmann, T.A., Bouvier, A.-S., Deloule, E., 2024. Olivine formation processes and fluid pathways in subducted serpentinites revealed by in-situ oxygen isotope analysis (Zermatt-Saas, Switzerland). Chem. Geol. 649, 121978. https://doi.org/10.1016/j.chemgeo.2024.121978.

Urann, B.M., Roux, V.L., John, T., Beaudoin, G.M., Barnes, J.D., 2020. The distribution and abundance of halogens in eclogites: an in situ SIMS perspective of the Raspas complex (Ecuador). 105, 307–318, doi:10.2138/am-2020-6994.

van Hunen, J., van den Berg, A.P., Vlaar, N.J., 2002. On the role of subducting oceanic plateaus in the development of shallow flat subduction. Tectonophysics 352, 317–333. https://doi.org/10.1016/S0040-1951(02)00263-9.

van Keken, P.E., Wada, I., Abers, G.A., Hacker, B.R., Wang, K., 2018. Mafic high-pressure rocks are preferentially exhumed from warm subduction settings. Geochem., Geophy., Geosys. 19, 2934–2961. https://doi.org/10.1029/2018GC007624.

Vesin, C., Rubatto, D., Pettke, T., 2024. The history of serpentinisation at mid-ocean ridges: insights from in situ trace elements coupled with oxygen and boron isotopes. Chem. Geol. 654, 122060. https://doi.org/10.1016/j.chemgeo.2024.122060.

Vogt, K., Gerya, T.V., 2014. From oceanic plateaus to allochthonous terranes: numerical modelling. Gondwana Res. 25, 494–508. https://doi.org/10.1016/j.gr.2012.11.002.

Warr, L.N., 2021. IMA–CNMNC approved mineral symbols. Mineral. Mag. 85, 291–320. https://doi.org/10.1180/mgm.2021.43.

Zhang, Y., Gazel, E., Gaetani, G.A., Klein, F., 2021. Serpentinite-derived slab fluids control the oxidation state of the subarc mantle. Sci. Adv. 7, eabj2515. https://doi.org/10.1126/sciadv.abj2515.